Materials and Design 160 (2018) 557–571

Contents lists available at ScienceDirect

Materials and Design

journal homepage: www.elsevier.com/locate/matdes

Particle-induced damage in Fe–TiB_2 high stiffness metal matrix composite steels

Ding Wang [a], Pratheek Shanthraj [a,b], Hauke Springer [a,*], Dierk Raabe [a]

[a] Max-Planck-Institut für Eisenforschung GmbH, Max-Planck-Straße 1, 40237 Düsseldorf, Germany
[b] The School of Materials, The University of Manchester, M13 9PL Manchester, UK

HIGHLIGHTS

- Crystal plasticity simulations of heterogeneous composite materials coupled with phase field damage model.
- The particle damage process can be predicted in the simulations.
- Effect of particle clustering degree, particle size and particle volume fraction discussed.
- Design strategies for high modulus steels with good damage tolerance derived.

GRAPHICAL ABSTRACT

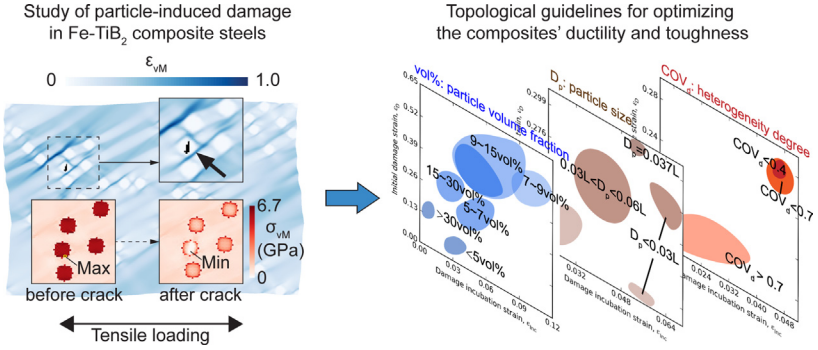

ARTICLE INFO

Article history:
Received 22 May 2018
Received in revised form 4 September 2018
Accepted 16 September 2018
Available online 18 September 2018

Keywords:
Metal matrix composites
Damage simulation
Particle damage
Phase field method
Spectral method

ABSTRACT

Fe–TiB_2 metal matrix composites, termed high modulus steels, have great potential for lightweight design applications due to their high stiffness/density ratio. However, the observed embrittlement, caused by the TiB_2 particles, critically limits application of these steels. Experimental studies to identify the influence of particle microstructure on ductility and toughness are complex in view of the multitude of parameters affecting microstructural damage. We therefore pursue instead an integrated computational materials engineering approach to gain understanding and derive guidelines for optimizing the particle microstructure and thus improve the mechanical properties, particularly the damage tolerance of these high modulus steels. Key microstructural parameters such as particle clustering degree, size and volume fraction were investigated. Model geometries were statistically and systematically generated with varied particle configurations from random to clustered distributions. Simulations were performed using a crystal plasticity Fast Fourier transformation method coupled with a novel phase field damage model. The influence of particle configuration on damage initiation and evolution was evaluated from the simulation results, and it was observed that microstructures with homogeneous particle distributions of 7 to 15 vol% TiB_2, devoid of large TiB_2 particles stemming from primary solidification, appear most favorable for obtaining high modulus steels with optimized mechanical properties.

1. Introduction

Metal matrix composites (MMCs) have enormous benefits for lightweight design in structural applications, such as transportation systems and machine components, as the addition of stiff lightweight ceramic

* Corresponding author.
E-mail address: h.springer@mpie.de (H. Springer).

https://doi.org/10.1016/j.matdes.2018.09.033

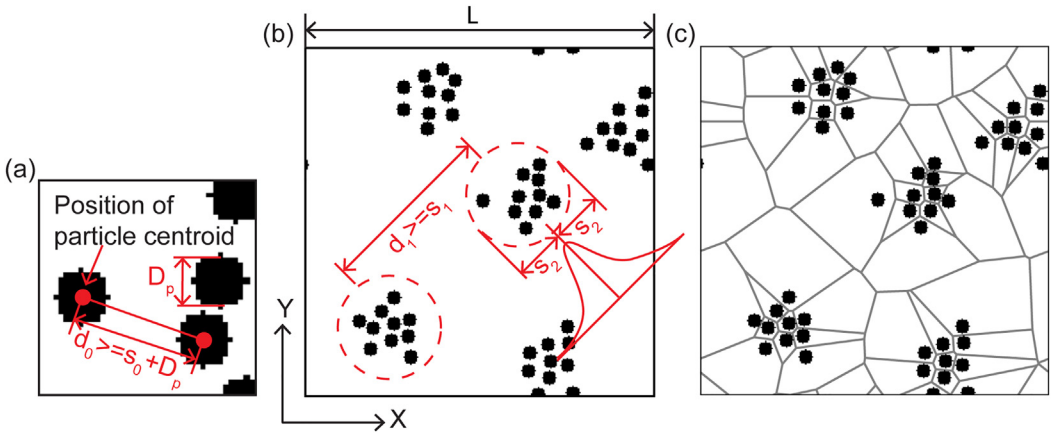

Fig. 1. Schematic of composite microstructure: (a) particle geometry, (b) microstructure of clustered distribution and (c) its Voronoi tessellation.

particles increases the specific stiffness (i.e. the stiffness/density ratio) of the material. Suitable stiff lightweight phases range from oxides, nitrides, carbides to borides, mostly in particulate or fibre form [1–3]. Fe-TiB_2 metal matrix composites (MMCs) have promising advantages, not only due to its mostly quasi-isotropic improvement of the specific stiffness, but also its low cost, high flexibility and availability to achieve excellence performance. Since TiB_2 is very hard, the initial application of Fe-TiB_2 MMCs was wear resistance steels [4,5]. Around 2000, Tanaka and Saito [6] investigated the potential of increasing the specific modulus of iron matrix by addition of TiB_2 particles. From that time, this novel type of steels was termed high modulus steels (HMS). HMS can be applied in the industry fields with strict design criteria of lightweight and high-stiffness target, for instance in automotive industry [7]. In addition, HMS also has great potential to be applied for heavy gauge materials for high performance cranes [8] and the material for wind turbine [9].

Previous studies have shown that the fabrication of MMCs via powder metallurgy synthesis techniques allows for precise control of the particle microstructure, but also requires great effort in material synthesis and thus high costs [10,11]. This production constraint could be overcome by utilizing liquid metallurgy synthesis [12,13], for which the iron (Fe) titanium di-boride (TiB_2) system is ideally suited [14]. TiB_2 is very effective in terms of stiffness (Young's modulus, E~565GPa) and density (ρ~4.25g cm^{-3}) [15] and can be formed in-situ from Fe-Ti-B melts. However, the large contrast in stiffness between particle and matrix as well as geometrical constraints imposed by particle morphology (i.e. sharp-edged shape) result in local stress concentrations, which promotes damage initiation such as cracks within particles, matrix or the associated interfaces. The newly formed sharp corners created from cracked particles create additional points of stress concentration. With increasing strain, large voids can thus form and result in damage progression [16,17]. For Fe–TiB_2 MMCs, synthesized in-situ from liquid melts, also termed high modulus steels (HMS), it was found that strong interfacial cohesion between the matrix and the reinforcing particles can be achieved [18–20]. A nanoindentation study conducted by Huang and co-workers [18] also reported that the TiB_2-matrix interfaces can be subjected to large plastic deformation which promotes interfacial compliance and bonding. Therefore, the damage mechanism of these MMCs is mainly attributed to the cracking of TiB_2 particle instead of interfacial de-bonding during uniform elongation [18,21,22].

This cracking of particles and the associated damage initiation into the adjacent matrix during deformation results in loss of composite toughness and ductility [23–26]. This issue poses a major concern in the application of such composites as structural materials. The complex microstructure of the reinforcements, such as large variations of particle size, morphology, dispersion, and volume fraction create an associated complexity in the partitioning of the internal stress and strain field across the matrix, thereby exerting a strong influence on particle cracking and the initiation and progression of damage [21,27]. It is possible to manipulate particle configuration, for example, by controlled solidification such as the decrease in particle size by fast solidification or rendering a regular distribution by eutectic remelting [14]. However, due to the multitude of interacting parameters and microstructural complexity, experimental efforts have so far been limited in clarifying the relationship between particle configuration and improved toughness. In order to reduce the work and cost associated with experimental microstructure optimization alone, additional systematic screening through simulation studies can be used to speed up this process by providing basic constitutive and morphological guidelines towards identifying favorable particle microstructures [28].

So far, the parametric studies regarding deformation and damage mechanisms in MMCs were mostly carried out in aluminium-matrix composites reinforced with alumina or silicon carbide. For instance, Segurado et al. [29,30], studied the effect of the particle spatial distribution on the mechanical behavior in model aluminium-alumina MMCs with up to 15 vol% of reinforcement. They found that the probability of particle fracture increases 3–6 times even for small degrees of particle clustering. Similar findings were also reported by Ayyar et al. [31] in a simulation study on aluminium-carbide MMCs. However, these studies focused only on small sets of samples and without systematic variation of particle configurations. Experimental studies on particle fracture in Al matrix composites [27,32–36] reported that composites containing larger particles are more likely to experience particle fracture during deformation. However, these studies did not consider the influence from particle distribution and particle size [37–39]. To reflect the full microstructure complexity of such compounds, we thus conducted a simulation study with systematically varied clustering degree, particle distribution and volume fraction to derive guidelines for particle microstructures that provide optimum mechanical performance. This integrated computational materials engineering (ICME) approach has the goal to identify key factors for particle damage initiation, growth and

Table 1
Values of the elastic stiffness of TiB_2 [58].

Property	Symbol	Value	Unit
Elastic constants for HCP lattice structure	C_{11}	656	GPa
	C_{12}	66	GPa
	C_{13}	98	GPa
	C_{33}	461	GPa
	C_{44}	259	GPa
	C_{66}	295	GPa
Ratio of lattice constants	c/a	1.0629	

Table 2
Crystal plasticity constitutive parameters of the elastic and plastic response of the ferrite matrix [61–63].

Property	Symbol	Value	Unit
Elastic constants for bcc lattice structure	C_{11}	233.3	GPa
	C_{12}	135.5	GPa
	C_{44}	118.0	GPa
Reference shear rate	$\dot{\gamma}_0$	0.001	s^{-1}
Initial and saturation slip resistance on {110} or {112} slip family, respectively	g_0, {110}	95	MPa
	g_∞, {110}	222	MPa
	g_0, {112}	97	MPa
	g_∞, {112}	412	MPa
Initial hardening coefficient	h_0	1	
Interaction coefficients	Coplanar $h_{\alpha\beta}$	1	
	Non-coplanar $h_{\alpha\beta}$	1.4	
Inverse shear rate sensitivity	n	20	
Numerical parameter	m	2.25	

percolation, in order to derive synthesis strategies for the next generation of HMS for lightweight applications.

2. Modelling strategy

In this study, different variations related to the particle clustering degree, particle size and particle volume fractions were studied. The simulations were performed with the multi-physics simulation package DAMASK [40,41] which provides a coupled crystal plasticity and phase field damage model [42]. A spectral solver was employed to solve the mechanical boundary value problem and the governing phase field kinetic evolution predicting the initiation and growth of particle damage.

2.1. Crystal plasticity

The crystal plasticity model used in this study is a phenomenological viscoplastic mean field dislocation rate formulation [43] to describe the behavior of the crystalline α-Fe bcc matrix. Kinematics is described in terms of the plastic velocity gradient, $\mathbf{L}_p = \dot{\mathbf{F}}_p \mathbf{F}_p^{-1} = \sum_\alpha \dot{\gamma}^\alpha \mathbf{b}^\alpha \otimes \mathbf{n}^\alpha$, which is determined by the superposition of the slip shear rates, $\dot{\gamma}^\alpha$, on each of the twelve ⟨111⟩{110} and the twelve additional ⟨111⟩{112} slip systems, which are indexed by $\alpha = 1, \ldots, 24$, where $\mathbf{b}^\alpha$ and $\mathbf{n}^\alpha$ are unit vectors along the slip direction and slip plane normal, respectively. The slip shear rate equations are given by $\dot{\gamma}^\alpha = \dot{\gamma}_0 |\frac{\tau^\alpha}{g^\alpha}|^n \operatorname{sgn}(\tau^\alpha)$. The plastic slip, $\dot{\gamma}^\alpha$, on a slip system α occurs when the resolved shear stress, $\tau^\alpha = \varphi^2 \mathbf{S} \cdot (\mathbf{b}^\alpha \otimes \mathbf{n}^\alpha)$, exceeds a critical value g^α. $\mathbf{S}$ is the applied second Piola-Kirchhoff stress and φ is the phase field damage variable. The slip resistance values, g^α, evolve asymptotically towards g_∞^β as a function of the shear on other slip systems γ^β ($\beta = 1, \ldots, 24$) according to the relationship $\dot{g}^\alpha = \dot{\gamma}^\beta h_0 |1 - \frac{g^\beta}{g_\infty^\beta}|^m \operatorname{sgn}(1 - \frac{g^\beta}{g_\infty^\beta}) h_{\alpha\beta}$, with initial hardening h_0 and a numerical strain hardening parameter m. The hardening matrix $h_{\alpha\beta}$ phenomenologically captures the interaction among the different slip systems.

2.2. Phase field damage model

To investigate the crack propagation process of the brittle particle in the MMC materials, we coupled a novel phase field method (PFM) derived for brittle fracture [42,44] with the crystal plasticity constitutive model. Shanthraj et al. [42] initially proposed and formulated this brittle fracture phase field approach for finite strain elasto-viscoplastic material, which is capable of successfully predicting physically realistic crack patterns when applied to a full field microstructure scenario and can be solved using a corresponding finite-element (FE) or spectral solver implementation. In the current study the model was further developed and implemented into a spectral method to handle the numerical solution of the coupled field equations [45]. The phase field variable is a scalar non-local damage variable φ varying between the initially undamaged ($\varphi = 1$) and fully damaged state ($\varphi = 0$). The damage evolution process is based on the variational theory of brittle fracture [46], and the method is closely related to gradient models employed in brittle [47,48] and ductile damage theory [49]. The stress relaxation associated with brittle damage is a result of a degradation of the material stiffness. The brittle damage evolution is driven by the continuous release of stored elastic energy at local material point, i.e. $\psi_E = \frac{1}{2}\varphi^2 \mathbf{S} \cdot \mathbf{E}$ ($\mathbf{E}$: elastic Green-Lagrange strain), from an undamaged state to a fully damaged state. As a resistance to the creation of crack surface, the associated

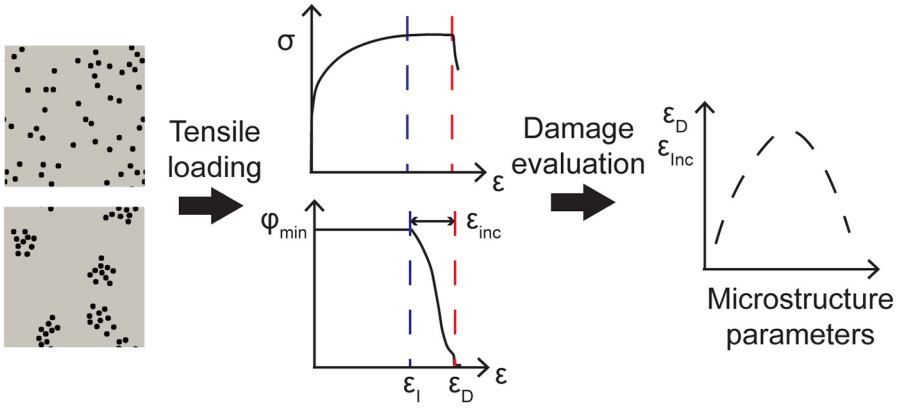

Fig. 2. Damage evaluation of the initial particle damage process in the simulations. From the evolution curve of the minimum damage field variable φ_{min} with global strain ε, three characteristic values were derived: the instability strain ε_I, the initial damage strain ε_D and the damage incubation strain ε_{Inc}. The characteristic values ε_D and ε_{Inc} are here exemplarily plotted as a function of certain microstructure parameters which are derived in the following analysis.

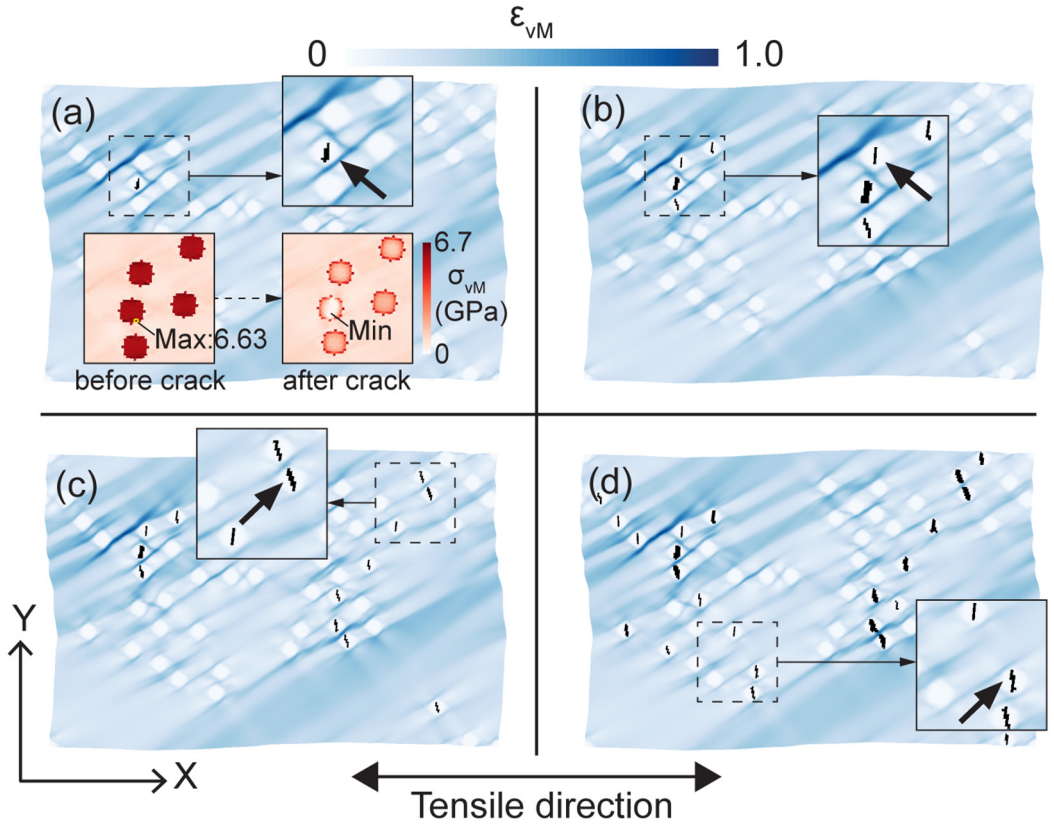

Fig. 3. Patterns of progressive particle damage (black area) coupled with von Mises true strain ε_{vM} distributions at successive global strains of: (a) 0.2461; (b) 0.2467; (c) 0.2473; (d) 0.2494. In (a), the von Mises true stress σ_{vM} distributions of the area including the earliest damage event are drawn at the loading step just before and after particle crack. The maximum stress point inside the particle before crack and the minimum stress point inside the particle after crack are indicated. The heterogeneity degree of the modelled microstructure is $COV_d \approx 0.55$ and the particle size is $D_p = 0.04$ L, where L is the side length of the RVE geometry. The details of particle damage are highlighted in magnified images and indicated by black arrows. The white blocky regions indicate positions where the hard particles are located.

damage surface energy takes the form of a Landau-type phase field approximation:

$$\psi_{surf} = \frac{G_0}{l_0}(1-\varphi) + G_0 l_0 |\nabla\varphi|^2 \tag{1}$$

with effective interface thickness, l_0, and critical energy density, G_0/l_0, of the interfacial region, and G_0 is associated with the fracture energy.

φ is modelled as a non-conservative structure phase field similar as in Allen-Cahn theory formulations. The evolution of φ results from the relaxation of the total free energy according to the classical (time-dependent) Ginzburg-Landau model [50]:

$$\dot{\varphi} = -M\left[2\varphi \mathbf{S}\cdot\mathbf{E} - \frac{G_0}{l_0} - \nabla G_0 l_0 \nabla\varphi\right] \tag{2}$$

with mobility M. Details about the phase field damage model and its coupling with crystal plasticity are described in detail in Refs. [42, 44].

2.3. Numerical solution

In our study, the simulations were conducted using a spectral method [51–53] based on the fast Fourier transform coupled to DAMASK. The use of a spectral method for solving the mechanical boundary value problem, which was pioneered by Moulinec and Suquet [54,55], was developed further by Lebensohn [56] and has since been developed further in computational material mechanics [57,58]. There are mainly two advantages associated with the spectral solution method in the context of the present constitutive laws and targeted simulation goals. One advantage is its straightforward use of periodic geometry of regularly arranged points. Such a geometry feature is not only convenient for generation of representative volume element (RVE) but can also be implemented without having to treat explicit border effects. The other advantage is its improved computational efficiency of

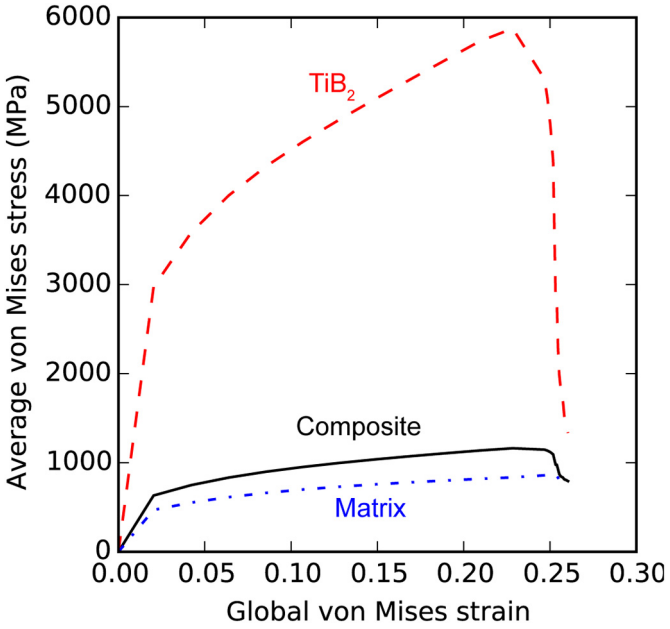

Fig. 4. Average von Mises stress versus Global von Mises strain for the TiB_2 particle, α-Fe matrix and Fe – TiB_2 composite.

heterogeneous materials compared to finite element method (FEM) because of its use of trigonometric polynomials as ansatz functions and also its repetitive operation of a fast FOURIER transform (FFT) which allows for a very time- and memory-efficient iterative solution algorithm [59]. This efficiency of spectral method over FEM has been demonstrated by previous studies [51,60,61]. For the application to heterogeneous materials with large contrast of local properties, the convergence was improved and accelerated greatly by several approaches developed in recent years, such as accelerated scheme [62], augmented Lagrangian scheme [63,64], polarization-based scheme [65] and efficient alternatives to the fix-point method [66,67]. The recent improvement of the computational efficiency of the spectral solver as coded in DAMASK, in particular with regards to applications to heterogeneous materials [52], make it particularly suited for MMC materials with large local stiffness contrast among the adjacent phases. In our study, we used the advanced constitutive laws which couple crystal plasticity and phase field damage model to simulate co-deformation of heterogeneous composite materials. Incorporating the above-mentioned advantages of spectral method, systematic study with more than hundred individual simulations can be conducted efficiently at low computational costs.

3. Simulation setup

3.1. Generation of the particle microstructure

To investigate the effects of different particle parameters on damage behavior, several microstructure variations were generated. In this study, two-dimensional periodic composite microstructures are built with simplifications such as uniform particle size, circular particle shape and single crystal ferritic matrix. For generating a random reference distribution, the particle centroid position (the red point indicated in Fig. 1a) was placed in the matrix following the random sequential adsorption (RSA) algorithm [29,30,68]. Particle i is placed if the distance

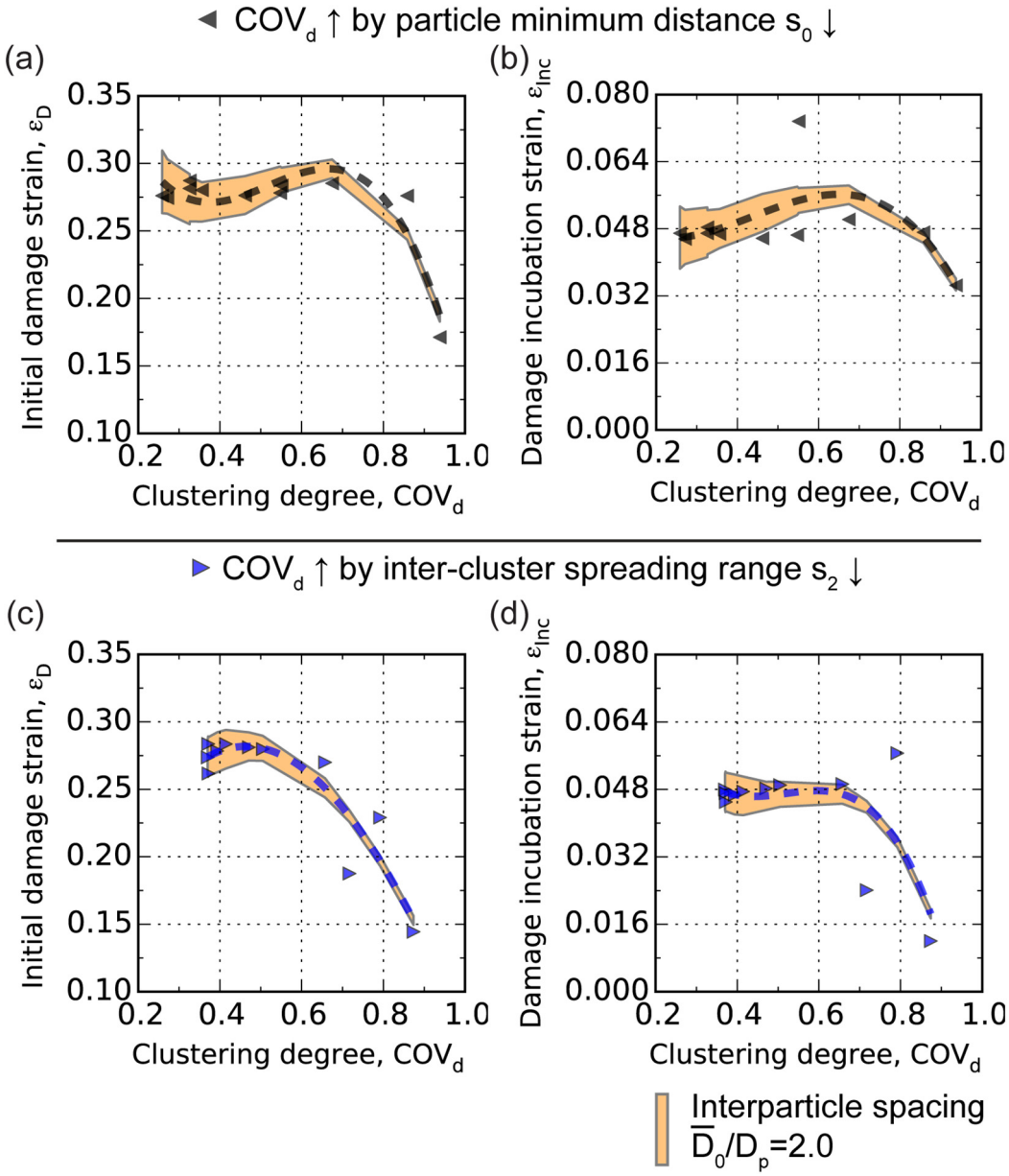

Fig. 5. The initial damage strain ε_D and damage incubation strain ε_{Inc} as function of the particle clustering degree COV_d. The increase of the clustering degree was achieved by either concentrating particles towards each other (a, b), or by shrinking the cluster size (c, d). The average interparticle spacing of the particle distribution is qualitatively represented by the height of the orange area. The reference height of the orange area, which is in the bottom of the figure, corresponds to $\overline{D}_0 = 2D_p$.

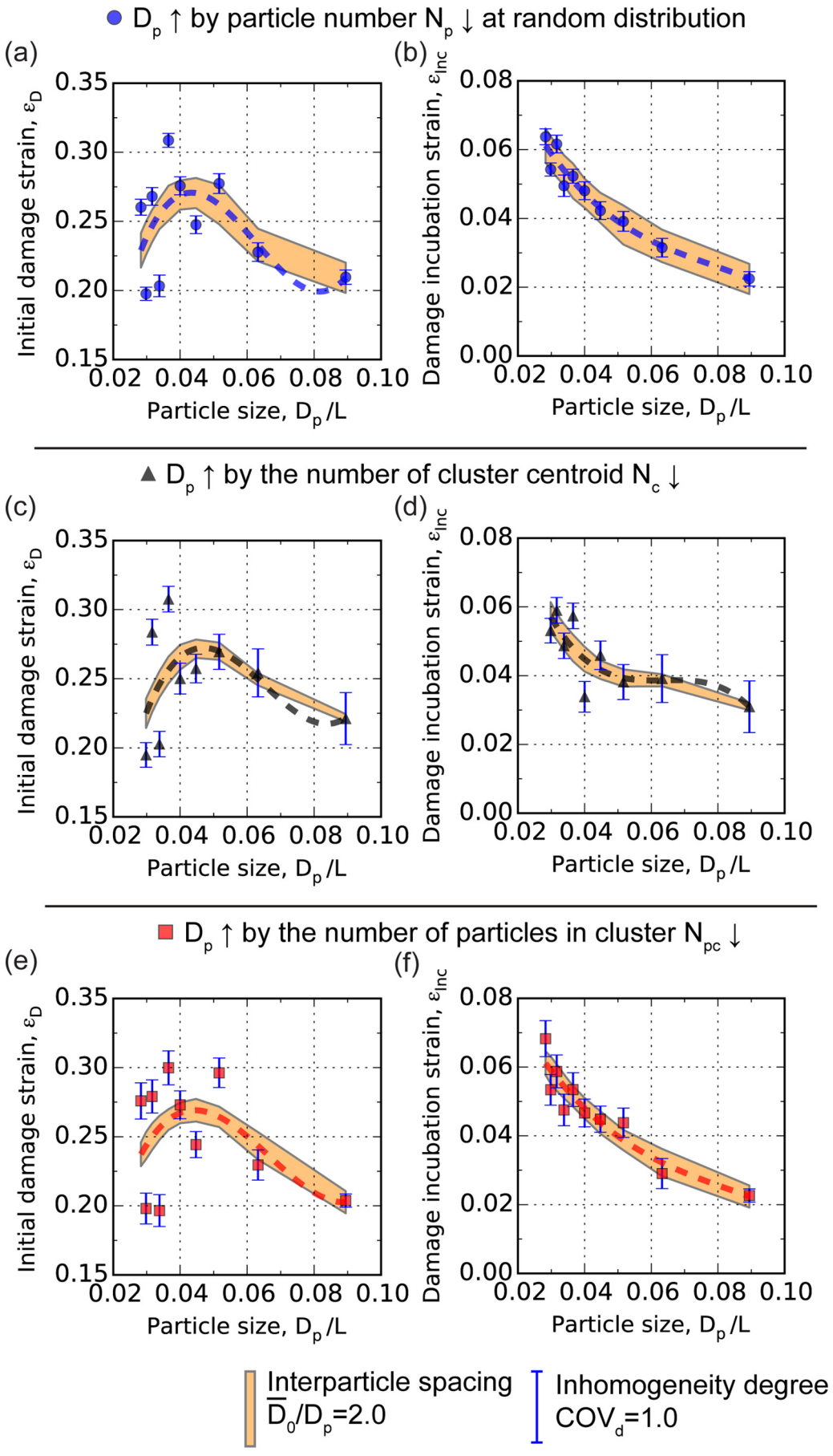
● D_p ↑ by particle number N_p ↓ at random distribution
(a)
(b)
Initial damage strain, ε_D
Damage incubation strain, ε_{Inc}
Particle size, D_p/L
▲ D_p ↑ by the number of cluster centroid N_c ↓
(c)
(d)
■ D_p ↑ by the number of particles in cluster N_{pc} ↓
(e)
(f)
Interparticle spacing
$\overline{D}_0/D_p$=2.0
Inhomogeneity degree
COV_d=1.0

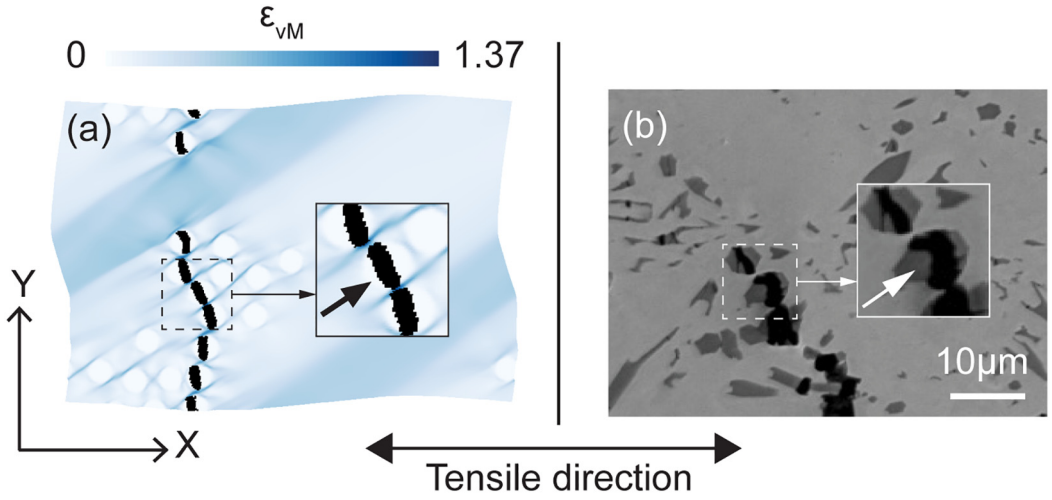

Fig. 7. Percolation of particle damage observed in simulations and also in experiment. (a) The simulated particle damage pattern (black area) is shown together with the von Mises equivalent strain ε_{vM} distribution at a macroscopic strain level of 23.02%. The heterogeneity degree of the modelled microstructure is $COV_d \approx 0.87$ and the particle size is $D_p = 0.063$ L. The detail of particle damage is highlighted in the magnified image and indicated by the black arrow. The white blocky regions indicate positions where the hard particles are located. (b) Experimental image showing damage percolation of fractured coarse particles in a longitudinal section close to the fracture zone. The total elongation is about 7%. The detail of particle damage is highlighted in the magnified image and indicated by the white arrow.

between this particle and all the other particles previously placed j = 1, …, i − 1 exceeds the sum of the minimum interparticle distance, s_0, and the particle diameter, D_p. If $\boldsymbol{x}_i$ stands for the centroid position of particle i, this condition is expressed as $d_0 = ||\boldsymbol{x}_i - \boldsymbol{x}_j + \boldsymbol{h}|| \geq s_0 + D_p, \quad \boldsymbol{h} = (h, k)$, where the parameters h and k can assume values of 0, L, −L, where L is the side length of the modelled RVE (representative volume element) geometry. The term D_p added on the right side is used for the boundary condition that particles cannot overlap. The vector $\boldsymbol{h}$, added on the left side, is used for implementing periodic boundary conditions of the RVE. That is, the particles being placed near to the RVE edge should also meet the minimum distance requirement from the particles adjacent to the opposite RVE edge. For generating an RVE with a clustered distribution of the hard inclusions (Fig. 1b), several cluster centroids N_c are placed at a minimum cluster distance s_1 using the same RSA process. About each cluster centroid, a specific number of particles N_{pc} are placed at distances derived in a way so as to match a normal distribution [69,70] with standard deviation s_2. This inter-cluster arrangement protocol also considers a certain prescribed minimum particle distance s_0 and the periodic boundary conditions imposed for the RVE simulations. Following these topological rules, the modelled particle microstructures can be well controlled in its key statistical features by adjusting these geometrical factors.

3.2. Heterogeneity quantification of the particle distribution

We quantified the degree of heterogeneity of the generated particle distributions in terms of the coefficient of variance of the mean near-neighbour distance (COV_d). Boselli and Yang et al. [70,71] found that the COV_d value, derived from a finite-body tessellation, was very sensitive to heterogeneity variations but essentially independent of particle morphology, size, orientation and volume fraction. In this study, we used Voronoi/Dirichlet tessellations to identify particle neighbours (Fig. 1c) and calculate the corresponding particle spacing based on the tessellation method used. COV_d is defined as:

$$COV_d = \frac{{s_d}^2}{d} \tag{3}$$

where ${s_d}^2$ is the variance of the mean near-neighbour distances of all particles and d is the average of the mean near-neighbour distances. Typically, the higher the COV_d, the more "clustered" the particles are. For a random particle distribution, the COV_d value is close to 0.36 [31,70].

3.3. Model parameters and simulation set-up

The TiB_2 phase is modelled as an elastic material with stiffness coefficients (as shown in Table 1) taken from first-principles pseudo-potential calculations by Milman et al. [72]. From that the fracture interface energy of the TiB_2 particles was calculated as $G_0 = {K_{IC}}^2 \Big/ E \approx 6\,8\ J \cdot m^{-2}$, where K_{IC} is the fracture toughness (around 6.2 MPa·$m^{1/2}$ [15]) and E is the Young's modulus (about 565GPa at 23 °C [72–74]) of the TiB_2 particles. The effective damage interface thickness l_0 was taken as 0.5 μm, corresponding to 2 Fourier points in the modelled geometry.

The crystal plasticity constitutive model parameters used for the α-Fe matrix was adopted from earlier works [75–77] (Table 2). The modelled 2D square composite representative volume element is discretized into an equidistance grid of 250 × 250 = 62,500 Fourier points. All the simulations were conducted under uniaxial tensile loading along the **X** direction. Uniaxial tension was applied at a rate of 0.01 s^{-1} with a time step of 0.01 s.

Fig. 6. The initial damage strain ε_D and damage incubation strain ε_{inc} as function of the relative particle size D_p/L. The increase of particle size is associated with reducing the particle number under constant volume fraction: (a, b) by reducing the particle number N_p at random distribution, (c, d) by reducing the number of cluster centroid N_c at inhomogeneous distribution, and (e, f) by reducing the number of particles about each cluster centroid N_{pc}. The average interparticle spacing $\overline{D}_0/D_p$ of the particle microstructure is qualitatively presented by the height of the orange area. The heterogeneity degree COV_d of the particle distribution is revealed by the length of blue error bar. Located in the bottom of the figure, the reference height of the orange area corresponds to $\overline{D}_0 = 2D_p$ and the reference length of the blue error bar represents $COV_d = 1.0$.

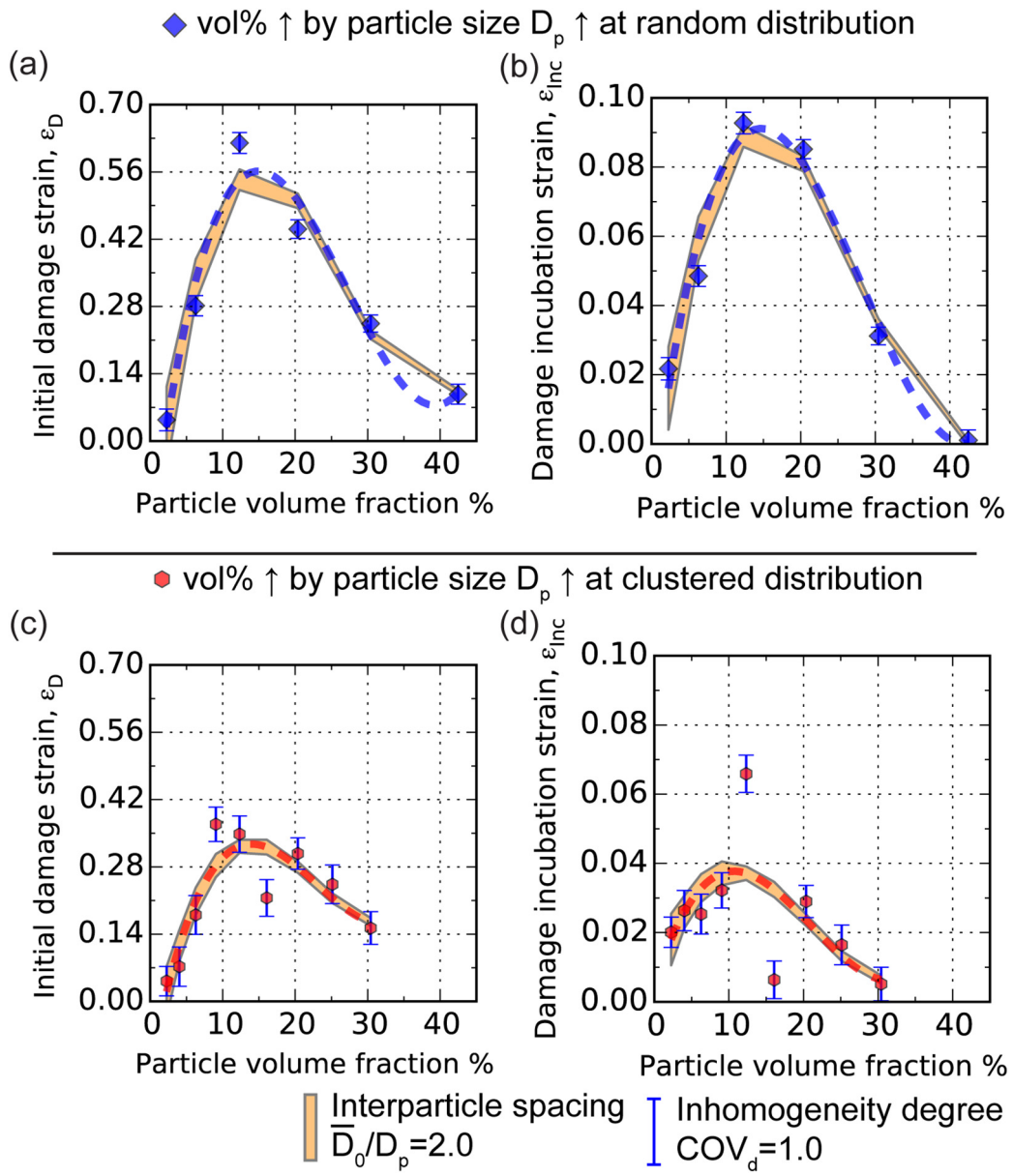

Fig. 8. The initial damage strain ε_D and damage incubation strain ε_{Inc} as function of the particle volume fractions. The increase of volume fraction was achieved by increasing particle size D_p: (a, b) at random distribution and (c, d) at clustered distribution.

3.4. Evaluation of initial particle damage

The process of initial particle damage is investigated to evaluate the influence of the degree of clustering, the average particle size and the volume fraction. An initial particle damage event is revealed by the drop of the damage field variable φ to its minimum value of zero. For evaluating this process, three characteristic metrics are extracted from the simulations as shown in Fig. 2. These are the instability strain, the initial damage strain and the damage incubation strain. The instability strain, ε_I, is the global strain value where the damage field variable starts to decrease below 1.0. This indicates that the particle becomes mechanically unstable and particle fracture is initiated. The initial damage strain ε_D is the global strain value when the damage field variable reaches zero, i.e. it marks the point of the earliest complete particle fracture event. This means there is one particle that becomes completely fractured and the associated flow stress σ of the composite starts to decrease due to the stress release of the damaged particle. The damage incubation strain $\varepsilon_{Inc} = \varepsilon_D - \varepsilon_I$ is the strain measure which represents the difference between the instability and damage strain, and it quantifies the toughness of the particle. Fig. 3 shows the characteristic values ε_D and ε_{Inc} and how they develop as a function of certain microstructure parameters which will be identified in the ensuing analysis. Such mechanisms are then used as a basis to identify the governing micromechanical structure-property relations to provide improved design guidelines for HMS with good ductility.

Fig. 9. The initial damage strain ε_D and damage incubation strain ε_{Inc} as function of the particle volume fractions. The increase of volume fraction was achieved by adding particles under three different ways: (a, b) by adding particles at random distribution, (c, d) by increasing the number of cluster centroids N_c, and (e, f) by increasing the number of particles about each cluster centroid N_{pc}.

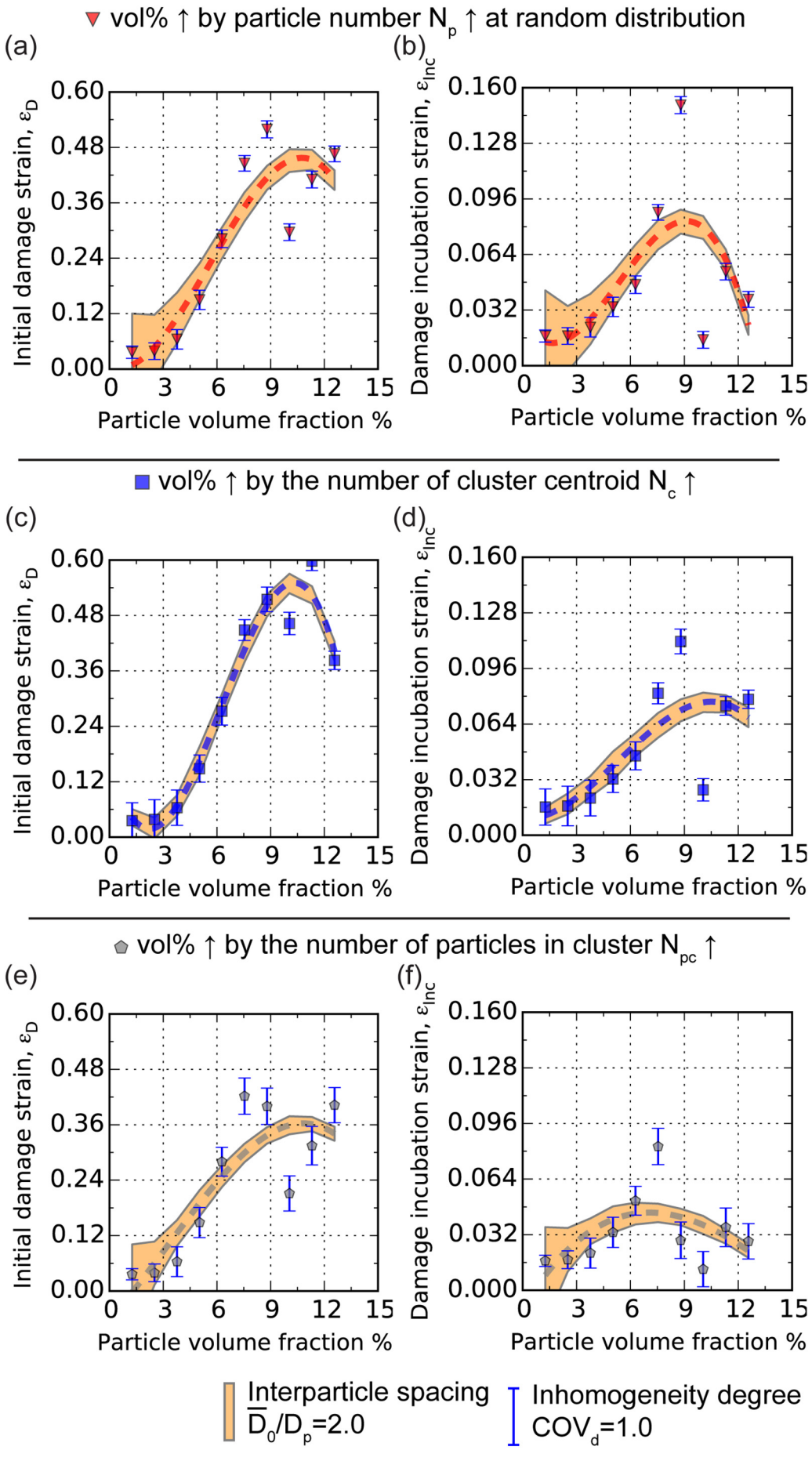
▼ vol% ↑ by particle number N_p ↑ at random distribution
(a)
(b)
Initial damage strain, ε_D
Damage incubation strain, ε_{Inc}
Particle volume fraction %
■ vol% ↑ by the number of cluster centroid N_c ↑
(c)
(d)
⬟ vol% ↑ by the number of particles in cluster N_{pc} ↑
(e)
(f)
Interparticle spacing
$\overline{D}_0/D_p$=2.0
Inhomogeneity degree
COV_d=1.0

4. Results

4.1. Example of particle damage patterns

The crystal plasticity simulations coupled with the phase field damage model are capable of predicting the particle damage process in the composite microstructure. This is revealed by an example of the simulated particle damage patterns (as shown in Fig. 3). The earliest particle fracture occurs at a macroscopic strain level of 0.2461 translating to strain localization levels up to around 1.0. The damage area inside the particles, where the local damage variable φ drops to zero, is shown in black color. To reveal the details of the individual particle damage events, the areas around the fractured particles are highlighted in the local enlarged images and the positions of the particle damage are indicated by the black arrows. For providing a micromechanical analysis of the earliest particle fracture event, the corresponding von Mises true stress σ_{vM} distributions are shown in the same enlarged area at the loading step both, just before and also after particle crack (Fig. 3a). The step before particle cracking is the stage before the local damage variable φ starts to decrease below a value of 1.0. At this step, a maximum stress peak of about 6.63 GPa is found inside the particle which will induce this earliest damage event. After cracking, the stress inside the particle decreases, especially for the damaged area where the point of minimum stress is found. This initial fracture event creates modulations of the local stress field, inducing adjacent load peaks and thus subsequent fracturing of neighboring particles as highlighted in Fig. 3b. With further loading, particle damage also percolates to other areas as indicated in Fig. 3c and d. At a macroscopic strain level of 0.2494 (Fig. 3d), about 55% of all particles are fractured. This process corresponds to the particle damage process observed in the damage evaluation experiment of the Fe – TiB_2 HMS [17]. To reveal the load transfer from matrix to particle, the average von Mises stress versus the global von Mises strain curves for the TiB_2 particle, α-Fe matrix and Fe–TiB_2 composite of this simulation example are plotted, respectively (Fig. 4). The results show that the average stress of the TiB_2 phase is one order of magnitude above that of the matrix. The TiB_2 particles are set to be only elastically deformed in the simulation. Once the α-Fe plastically deforms, the non-linearity in the evolution of the average stress for the TiB_2 is observed due to changes in local load transfer between the TiB_2 particles and the α-Fe matrix. The decrease in stress for the TiB_2 phase is due to the progressing particle damage process which translates at a macroscopic level at a gradual decay in its overall load bearing capacity.

4.2. Increasing the degree of particle clustering

To study the clustering degree effect, we considered only the change in the particle spatial distribution keeping the particle size and particle number constant. The relative particle diameter is $D_p = 0.04$ L. The total particle number is 50 with 5 clusters each containing 10 particles. In this study, the heterogeneity degree COV_d is used to quantify the clustering degree of particle distribution. The values of the particle size and particle numbers were varied so as to cover a large range of the COV_d from about 0.26 to 0.94. The minimum cluster distance s_1 was set to $6D_p$. The increase of the clustering degree was achieved by either reducing the interparticle spacing (the particle minimum distance s_0 decreased from $1.6D_p$ to $0.1D_p$), or by shrinking the cluster size (the inter-cluster spread s_2 decreased from $5D_p$ to $0.7D_p$). As shown in Fig. 5, the average interparticle spacing of the particle distribution is qualitatively presented by the height of the orange area. It shows that the interparticle spacing decreases significantly from about $1.8D_p$ to nearly $0.2D_p$ with the increase of the clustering degree. For this microstructural change, the simulations yield early and rapid particle fracture for the case of a high clustering degree. Fig. 5 quantifies this result in terms of the variation of the initial damage strain ε_D and damage incubation strain ε_{Inc} as function of the clustering degree COV_d. For cases of homogeneous and random particle distribution with COV_d values below 0.4, the initial damage strain ε_D stabilize in a range of about 0.27 and the damage incubation strain ε_{Inc} is about 0.048. Correspondingly for a clustering degree COV_d above 0.7 (interparticle spacing below $0.5D_p$), the trends of ε_D and ε_{Inc} (dashed lines) both decrease as the clustering degree increases. The trend of ε_D decreases to around 0.15 (at $COV_d \approx 0.87$ in Fig. 5c), i.e. about 50% lower strain values than that of homogeneous distributions. Meanwhile the trend of ε_{Inc} drops to nearly 0.016 (at $COV_d \approx 0.87$ in Fig. 5d), about 67% lower strain values.

4.3. Increasing the particle size

For a given volume fraction, a change in the particle size is tied to a corresponding inverse change in the particle number. In real MMC microstructures, the particle size change is always correlated with spatial distribution change due to the specific processing conditions. For instance, in HMS, the large primary particles having size > 10 μm tend to cluster together [78] and the small eutectic particles with approximately 1 μm width are more likely to disperse homogeneously [14]. Therefore, to simulate this change, a wide range of distributions were considered for the study of a particle size effect. As shown in Fig. 6, the heterogeneity degree COV_d and the average interparticle spacing of the particle distribution are qualitatively presented by the length of blue error bar and the height of the orange area respectively. The particle size is described here as a ratio D_p/L (abscissa values in Fig. 6) where D_p is the particle diameter. In this study, the particle size D_p increases from about 0.03 L to 0.09 L with the decrease of particle number from 100 to 10 under constant volume fraction. For the generation of the modelled particle microstructure, we considered three different routes to increase particle size: (i) reducing the particle number N_p (from 100 to 10) in random distribution; (ii) reducing the number of cluster centroids N_c (from 9 to 1, each cluster contains 10 particles) in the inhomogeneous distribution; and (iii) reducing the number of particles about each cluster centroid N_{pc} (from 20 to 2, the number of cluster centroid N_c fixed at 5). In this way, almost each particle size can have three different distributions to compare.

Similar values and trends of damage behavior with particle size change were obtained from these three groups except for some differences caused by high clustering degree. Fig. 6 quantifies the results in terms of the variation of ε_D and ε_{Inc} as function of the particle size D_p/L. As shown in Fig. 6a, c and e, the trend of ε_D (dashed lines) increases initially with fluctuation (about 0.1 strain values) to the peak value of about 0.27 at the particle diameter D_p range of 0.03–0.06 L. The peak value of ε_D corresponds to a particle diameter of 0.037 L. After the peak value, ε_D decreases continuously to a value of about 0.2 with the increase of particle diameter from 0.06 L to 0.09 L. As shown in Fig. 6b, d and f, ε_{Inc} decreases monotonically from about 0.07 to 0.02 with the increase of particle diameter D_p from about 0.03 L to 0.09 L.

In this study, for particle diameters D_p above 0.06 L, we found in highly clustered distributions (i.e. COV_d above 0.7), that the particles tend to fracture along a specific continuous pathway in the direction perpendicular to the tensile direction, resulting in particle damage percolation. This is exemplarily shown for a modelled microstructure in Fig. 7a. The detail of particle damage is highlighted in the magnified image and indicated by the black arrow. This is consistent with an experimental observation made on a ruptured tensile sample: The material probed here is a high modulus steel with 20 vol% TiB_2, prepared in a vacuum induction furnace under argon, cast into a 40 mm thick water-cooled mould followed by hot rolling. Tensile tests were conducted along the rolling direction at a constant crosshead speed of 5 um s^{-1}, corresponding to an initial strain rate of 10^{-3} s^{-1}. The image of the area close to fracture surface was taken by a field emission scanning electron microscope (SEM; JEOL-6500F, operated at 15 kV). As shown in the SEM image (Fig. 7b), in a longitudinal section close to the fracture zone, the damage percolation among the closely packed

coarse particles is observed. The fracture of the coarse particles is highlighted in the enlarged image and indicated by the white arrow. This correspondence not only validates our simulation results, but also demonstrates that clustered distributions with large particles tend to result in damage percolation during loading, an effect which greatly promotes failure of such MMCs.

4.4. Increasing the particle volume fraction

To study the effect of particle volume fraction, we considered changes resulting from a variation of both the size and number of particles. For TiB_2 above 12 vol% (~6.3 mol%), the Fe-TiB_2 alloy is above the eutectic TiB_2 concentration (pseudo-binary eutectic reaction [79]), and as a consequence, the average particle size increases significantly as large particles are formed during primary solidification. In this study, such changes correspond to the first route (Fig. 8) to increase the particle volume fraction from 2.26 vol% to 42.47 vol% by increasing particle size D_p (from 0.024 L to 0.104 L) in form of both, random and clustered distributions. For TiB_2 below 12 vol%, the matrix contains fine eutectic TiB_2 particles of similar size [80]. Thus, this process corresponds to the second route (Fig. 9) of increasing the particle volume fraction from 1.26 vol% to 12.57 vol% by increasing particle number. In this approach, the particles of constant diameter ($D_p = 0.04$ L) are added into the RVE in different ways, namely, by either (i) increasing the particle number from 10 to 100 at random distribution; or by (ii) increasing the number of cluster centroids N_c from 1 to 10 with each cluster containing 10 particles; or by (iii) increasing the number of particles about each cluster centroid N_{pc} from 2 to 20 with the number of cluster centroid N_c fixed at 5. By these topological rules, diverse particle distributions were introduced into the RVE.

Figs. 8 and 9 show the simulation results in terms of the variation of the initial damage strain ε_D and damage incubation strain ε_{Inc} as function of the particle volume fraction. The curve for ε_D (dashed lines) increases from about 0.02 to the peak values (between 0.3 and 0.6 strain values in different cases) as the volume fraction increases from 1.26% (Fig. 9a, c, e) or 2.26% (Fig. 8a and c) to the range of 7–15%. After the peak values, the ε_D decreases below 0.2 as the volume fraction increases above 30% (Fig. 8a and c). A similar trend is also observed for the variation of ε_{Inc}. Figs. 8 and 9 also show that the peak values of ε_D and ε_{Inc} for the homogeneous distributions (COV_d below 0.4) are about 30% above those for the inhomogeneous distributions (COV_d above 0.4), indicating significantly higher performance of such microstructures regarding particle damage for the more homogeneous distributions.

The volume fraction effect on the load transfer from matrix to particle is illustrated in the average von Mises stress versus global von Mises strain curves of the TiB_2 particle, α-Fe matrix and Fe–TiB_2 composite (Fig. 10). Fig. 10(a) shows that the TiB_2 particles are subjected to a decreasing level of the average stress from 5GPa to 1GPa with increasing volume fraction from 2.26% to 42.47%, especially during the elastic deformation of the composite. This is because a large fraction of the load

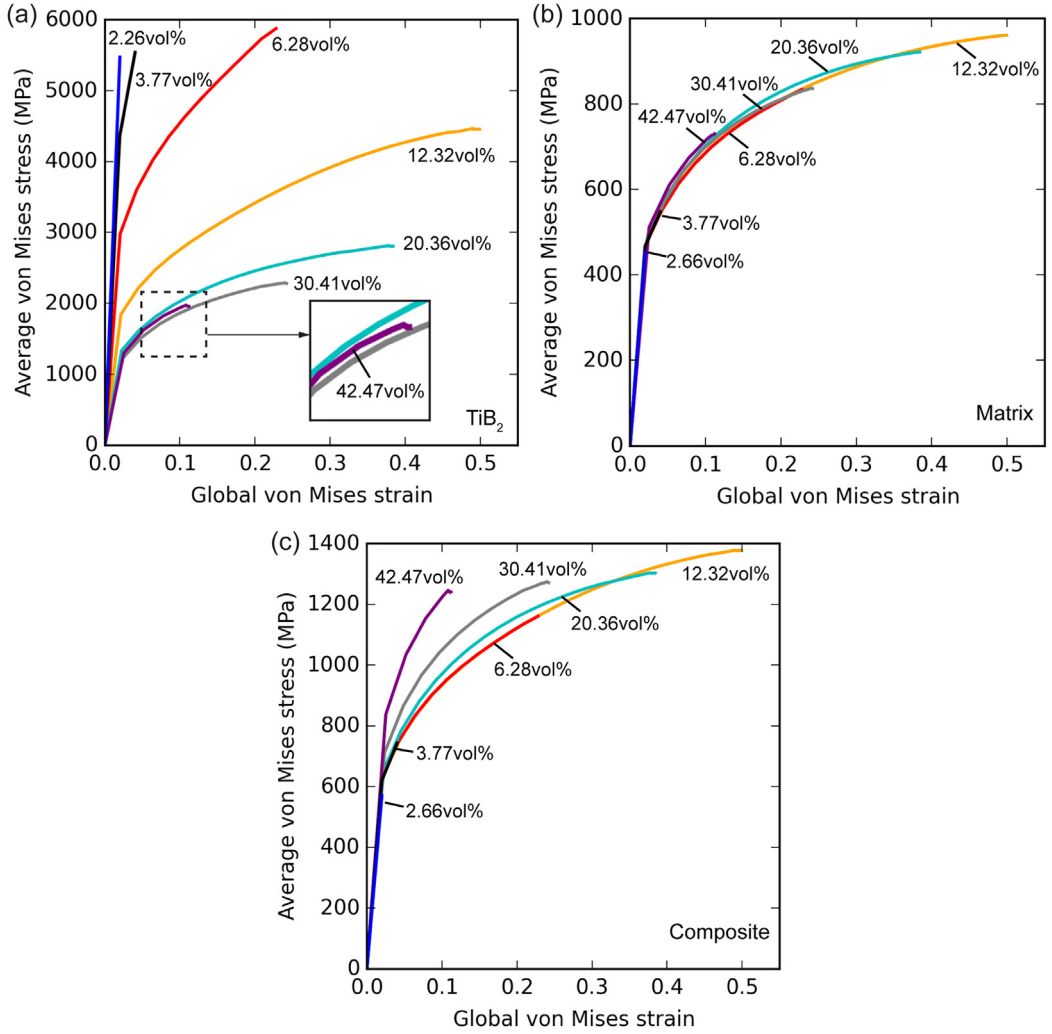

Fig. 10. For the composite microstructures with different TiB_2 volume fractions, the average von Mises stress versus Global von Mises strain curves are plotted before initial particle damage for (a) the TiB_2 particles, (b) α-Fe matrix and (c) Fe – TiB_2 composite. The particle distributions of the composite microstructures are homogeneous with $COV_d < 0.4$.

is carried by the overall higher reinforcement volume [38]. However, as the volume fraction increases further, the particles will carry more deformation as the matrix volume decreases. For 2.26% and 3.77%, the average stress level of the TiB_2 reaches peak values above 5GPa at a very early loading stage (viz, already at a global strain below 3%). This will promote the early onset of particle fracture. For 42.47 vol%, the average stress of the TiB_2 is a little higher than that for the 30.41 vol% specimen (magnified image in Fig. 10a). For the stress-strain curves of the matrix (Fig. 10b), not much difference is observed between the cases probed with different volume fractions. For the stress-strain curves of the composite (Fig. 10c), the strength increases significantly for high-volume fractions above 20 vol%.

5. Discussion

One of the main challenges for enabling Fe–TiB_2 HMS as lightweight materials lies in improving their ductility and toughness by minimizing particle-induced damage. This can be achieved by tailoring the particle microstructure, such as spatial distributions, size and volume fraction, according to their individual effects on the overall particle-induced damage behavior. In this study, our results allow to systematically evaluate the effects of different particle parameters in view of their suitability for composite design of high performance on particle damage behavior. This is revealed in Fig. 11, where values characteristic for evaluating particle damage, i.e. the initial damage strain ε_D and the damage incubation strain ε_{Inc}, are summarized. The ideal particle damage behavior is represented by simultaneously high values of ε_D and ε_{Inc}. Consequently, areas of ε_D vs ε_{Inc} for diverse groups of particle parameters are indicated in this modified Ashby map as the basis for discussing the effects observed.

5.1. Effect of particle clustering degree

We used the heterogeneity degree COV_d to quantify the clustering degree of the studied particle distributions. Even random distributions contain already several closely packed regions. In clustered distributions, this situation becomes more severe as the average interparticle spacing is significantly decreased (Fig. 5). Our current study covers a broad range of statistically relevant configurations with a total of 22 microstructures, varying the clustering degree COV_d from about 0.26 to 0.94. This allows us to determine critical values for particle clustering. Another important progress of this study lies in the use of advanced constitutive laws which couple crystal plasticity and phase field damage model to simulate co-deformation of heterogeneous composite materials. As illustrated in Fig. 11a, the particle distributions with COV_d

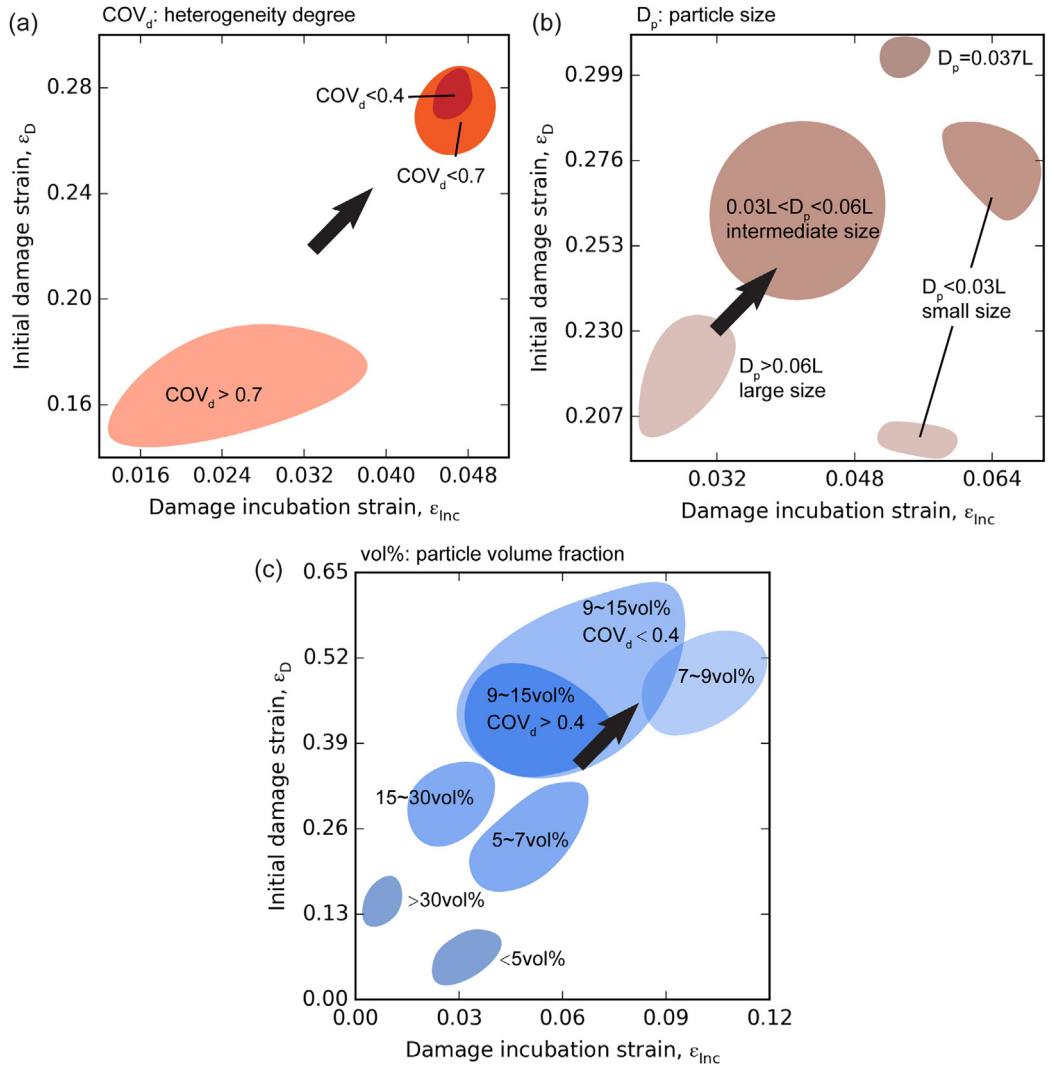

Fig. 11. Ashby-type diagrams for the characteristic parameters for evaluating the individual particle damage phenomena and their role for the design of high stiffness composite steels. Here focus is placed on the initial damage strain ε_D vs. damage incubation strain ε_{Inc} for different effects of particle parameters: (a) heterogeneity degree COV_d, (b) particle size D_p, (c) particle volume fraction vol%. The design directions for obtaining high performance on particle damage behavior are indicated by the black arrows. L: the side length of the modelled RVE geometry.

below 0.4 show optimal performance with high values of initial damage strain ε_D and damage incubation strain ε_{Inc}. However, the distributions with COV_d above 0.7 exhibit much lower values of ε_D and ε_{Inc}, which indicates a significantly increasing preference for particle fracture in highly clustered microstructures. This corresponds well to the experimental observation in the study by Zhang el al [78]. They showed that particle fracture events were concentrated in regions of a high degree clustering, especially in the area close to the material fracture surface. Similar observations were made in highly clustered areas by Szczepaniak el al [81]. In other systems, such as Al-SiC composites, studies on the effect of particle spatial distribution also revealed that the particle fracture probability significantly increased in very inhomogeneous microstructure both in experiments [82–85] and simulations [29–31].

5.2. Effect of particle size

From the analysis of simulation results (Figs. 6 and 11b), we found that particle damage is sensitive to the particle size. Our study revealed that particles fractured early and rapidly with large particle size (above 0.06 L). This corresponds well to the experimental observations by Hadjem-Hamouche et al. [17,86] and Li et al. [21] which showed that the large primary TiB_2 particles were fractured more frequently than the small eutectic particles. In their studies, the main damage initiation mechanism was dominated by the fracture of the coarse primary particles. This is due to that a larger load transfer from the matrix to the particle for large particles [16,37,38]. Similar observations were also found in Al-SiC composites [16,37,87]. From the damage pattern comparison between simulation and experiment in our study (Fig. 7), the good correspondence of shape and orientation of particle cracks can not only validate our simulation results, but also demonstrate that the clustered large particles tend to result in damage percolation during loading which could induce failure of MMCs. As illustrated in Fig. 11b, the intermediate particle size (0.03–0.06 L) in our study exhibited relatively good and stable damage performance. The optimal performance is observed at a specific particle diameter D_p of 0.037 L. With further decreasing particle size (below 0.03 L), large fluctuation was observed which splits into two sub-areas with different damage performance. This indicates that the small particles are more sensitive to the partitioning of the internal stress and strain field across the matrix. Therefore, corresponding alloy design efforts should be directed towards the intermediate particle size for obtaining stable performance on particle damage behavior and for avoiding producing any large particles.

5.3. Effect of particle volume fraction

Compared to the effects of particle clustering degree and particle size, the simulation results (Figs. 8 and 9) show that the particle volume fraction has the most significant impact on particle damage. As summarized in Fig. 11c, it reveals that the optimal performance on particle damage is in the range of 7–15 vol% with a homogeneous particle distribution (COV_d below 0.4). The volume fractions of Fe-TiB_2 MMCs fabricated by liquid metallurgy synthesis in previous studies were typically in the range of 10–20 vol% [14,17,78,80,86]. It was reported [80] from the experimental tensile testing that the Fe-TiB_2 composites with 10 vol% TiB_2 exhibits higher ductility with 48% tensile elongation (TE) than the composites with 20 vol% TiB_2 which shows only 15% TE. Our results correspond well to this trend as shown in Figs. 8 and 10c. For higher particle volume fractions, our study showed the composite exhibits very poor damage performance. In experiment, Tanaka et al. [6] reported that they fabricated Fe-TiB_2 composites – but via powder metallurgy synthesis – by incorporating about 30 vol% TiB_2 in an Fe-Cr alloy, however such composites are often brittle and exhibit relatively poor fracture properties [88]. For low volume fraction (<5 vol%), little attention was paid by research and engineering because such small reinforcement volume cannot achieve significant improvement of physical and mechanical properties.

5.4. Effect of particle interface

The interface between TiB_2 particle and Fe matrix plays a key role to achieve significant composite effect on strengthening and good enough ductility during deformation. This is because the interface is responsible for carrying the load between the matrix and the particles [16]. According to previous experimental investigations, good interfacial coherency and high interfacial strength were found [18–20,89] for Fe-TiB_2 MMCs fabricated by eutectic solidification. In addition, the recent studies [17,21,26,86,90] on the deformation behavior and damage evolution of Fe-TiB_2 MMCs showed that particle fracture is the dominating damage mechanisms and the main reason for damage failure of the composite at room temperature, whereas particle interface debonding is rarely and much less frequently observed. Therefore, the effect of interface decohesion on the damage behavior of Fe-TiB_2 MMCs is negligible. Because of this reason, we regard good interfacial bonding of Fe-TiB_2 interface as assumption and did not introduce the mechanism of interfacial decohesion in the study. As a result, the particle fracture is the major damage mechanism in our study which corresponds well to the experimental observations in Fe-TiB_2 composites (as shown in Fig. 7).

In our study, the direct strengthening resulted from the load transfer from matrix to particle is obvious. As shown in Fig. 4, the average stress of the TiB_2 particles is about one order of magnitude higher than that of the matrix. For the volume fraction effect, as illustrated in Fig. 10c, the strengthening increases with volume fractions. This is mainly due to more load transfer from matrix to particles as particle volume increases. Meanwhile, the average stress of the matrix did not change much (Fig. 10b). Such strengthening effect corresponds well to the previous studies [38,91]. However, although the strength of the composites can be improved greatly by increasing particle volume fraction, the ductility could be reduced significantly by the early onset of particle fracture (Figs. 8 and 10c) as the poor damage performance for high volume fractions (>30 vol%).

6. Summary and conclusions

The aim of this study is to provide topological guidelines for damage tolerant particle configurations for Fe–TiB_2 composites with the specific aim to optimize the composites' ductility and toughness by minimizing particle-induced damage. We systematically investigated the effects of different particle parameters, such as spatial distributions, size and volume fraction, on particle damage initiation and evolution under uniaxial tensile loading, using advanced constitutive approaches, namely, a coupled crystal plasticity – phase field damage model. The following conclusions are drawn:

(1) By using the spectral method, the computational efficiency of heterogeneous material can be greatly improved. The recent improvement of the computational efficiency of the spectral solver as coded in DAMASK make it particularly suited for MMC materials with large local stiffness contrast among the adjacent phases. Incorporating the advanced constitutive laws which couple crystal plasticity and phase filed method to simulate co-deformation of heterogeneous composite materials, this simulation method in our study can open pathways to the ICME approach with high-throughput simulations, which can further significantly speed up the material design process of the novel heterogeneous material with superior properties.
(2) For the effect of particle clustering, our study revealed a significantly increasing preference for early and rapid particle fracture in highly clustered microstructures, especially for COV_d values above 0.7. In homogeneous distributions (COV_d below 0.4), the simulation results showed a significantly high performance on particle damage.
(3) For the effect of particle size, our study revealed that particles fractured early and rapidly with large particle size (above

0.06 L). Composites with intermediate particle size (0.03–0.06 L) showed relatively good and stable damage performance. The optimal performance was observed at a specific particle diameter D_p of 0.037 L. Composites with small particle size (below 0.03 L) exhibited large fluctuation of damage behavior.

(4) For the effect of particle volume fraction, our study revealed that the particle volume fraction has the most significant impact on particle damage, comparing to the particle clustering and particle size. Our study showed the optimal damage performance is in the range of 7–15 vol% with a homogeneous particle distribution (COV_d below 0.4). Very poor damage performance was found for high volume fractions (>30 vol%) and very low volume fractions (<5 vol%). The particle volume fraction also has strong influence on composite strengthening. Due to the load transfer from matrix to particles, our study showed significant strengthening occurs for volume fraction higher than 30 vol%. However, the ductility could be reduced greatly due to very poor damage performance in such high volume fraction composites.

(5) From the analysis of simulation results, the above guidelines correspond well to the observations from previous experimental studies. Therefore, more pathways could be opened and further novel design of Fe-TiB_2 composites can be conducted based on the findings in this study. In summary, we recommend that Fe–TiB_2 HMS microstructures for optimum ductility and toughness should contain preferably homogeneous particle distributions (COV_d below 0.4) with 7–15 vol% and avoid large primary TiB_2 particles.

CRediT authorship contribution statement

Ding Wang: Developed and performed the simulations, Wrote the paper, Discussed the results and commented on the manuscript. **Pratheek Shanthraj:** Designed the research, Developed and performed the simulations, Wrote the paper, Discussed the results and commented on the manuscript. **Hauke Springer:** Designed the research, Discussed the results and commented on the manuscript. **Dierk Raabe:** Discussed the results and commented on the manuscript.

Acknowledgements

This work was supported by the doctoral grant given by the Max-Planck-Institut für Eisenforschung GmbH. The authors thank Dr. Han Zhang for providing experimental images on damage percolation.

References

[1] J.E. Allison, G.S. Cole, Metal-matrix composites in the automotive industry: opportunities and challenges, JOM 45 (1) (1993) 19–24.
[2] J.W. Kaczmar, K. Pietrzak, W. Włosiński, The production and application of metal matrix composite materials, J. Mater. Process. Technol. 106 (1–3) (2000) 58–67.
[3] D.B. Miracle, Metal matrix composites – From science to technological significance, Compos. Sci. Technol. 65 (15) (2005) 2526–2540.
[4] R. Telle, G. Petzow, Strengthening and toughening of boride and carbide hard material composites, Mater. Sci. Eng. A 105–106 (Part 1) (1988) 97–104.
[5] L.S. Sigl, K.A. Schwetz, TIB2-based cemented borides - a new generation of hardmetals, Powder Metall. Int. 23 (4) (1991) 221–224.
[6] K. Tanaka, T. Saito, Phase equilibria in TiB2-reinforced high modulus steel, J. Phase Equilib. 20 (3) (1999) 207.
[7] F. Bonnet, V. Daeschler, G. Petitgand, High modulus steels: new requirement of automotive market. How to take up challenge? Can. Metall. Q. 53 (3) (2014) 243–252.
[8] H. Berns, W. Theisen, Eisenwerkstoffe - Stahl und Gusseisen, Springer, 2006.
[9] H. Springer, C. Baron, A. Szczepaniak, V. Uhlenwinkel, D. Raabe, Stiff, light, strong and ductile: nano-structured High Modulus Steel, Sci. Rep. 7 (1) (2017) 2757.
[10] M.F. Ashby, Materials Selection in Mechanical Design, Third ed. Butterworth-Heinemann, Burlington, MA, USA, 2005.
[11] H. Nakanishi, K. Kakihara, A. Nakayama, T. Murayama, Development of aluminum metal matrix composites (Al-MMC) brake rotor and pad, JSAE Rev. 23 (3) (2002) 365–370.
[12] P.K. Rohatgi, R. Asthana, S. Das, Solidification, structures, and properties of cast metal-ceramic particle composites, Int. Met. Rev. 31 (1) (1986) 115–139.
[13] Y. Feng, Strengthening of Steels by Ceramic Phases, Fakultät für Georessourcen und Materialtenik, RWTH, Aachen, 2013.
[14] H. Springer, R. Aparicio Fernandez, M.J. Duarte, A. Kostka, D. Raabe, Microstructure refinement for high modulus in-situ metal matrix composite steels via controlled solidification of the system Fe–TiB2, Acta Mater. 96 (2015) 47–56.
[15] R.G. Munro, Material properties of titanium diboride, J. Res. Natl. Inst. Stand. Technol. 105 (5) (2000) 709–720.
[16] N. Chawla, Y.L. Shen, Mechanical behavior of particle reinforced metal matrix composites, Adv. Eng. Mater. 3 (6) (2001) 357–370.
[17] Z. Hadjem-Hamouche, J.-P. Chevalier, Y. Cui, F. Bonnet, Deformation behavior and damage evaluation in a new titanium diboride (TiB2) steel-based composite, Steel Res. Int. 83 (6) (2012) 538–545.
[18] M.X. Huang, B.B. He, X. Wang, H.L. Yi, Interfacial plasticity of a TiB2-reinforced steel matrix composite fabricated by eutectic solidification, Scr. Mater. 99 (2015) 13–16.
[19] S. Lartigue-Korinek, M. Walls, N. Haneche, L. Cha, L. Mazerolles, F. Bonnet, Interfaces and defects in a successfully hot-rolled steel-based composite Fe–TiB2, Acta Mater. 98 (2015) 297–305.
[20] L. Cha, S. Lartigue-Korinek, M. Walls, L. Mazerolles, Interface structure and chemistry in a novel steel-based composite Fe–TiB2 obtained by eutectic solidification, Acta Mater. 60 (18) (2012) 6382–6389.
[21] Y.Z. Li, Z.C. Luo, H.L. Yi, M.X. Huang, Damage mechanisms of a TiB2-reinforced steel matrix composite for lightweight automotive application, Metall. Mater. Trans. E 3 (3) (2016) 203–208.
[22] N. Chawla, J.W. Jones, C. Andres, J.E. Allison, Effect of SiC volume fraction and particle size on the fatigue resistance of a 2080 Al/SiC p composite, Metall. Mater. Trans. A 29 (11) (1998) 2843–2854.
[23] Z. Kulikowski, T.M.T. Godfrey, A. Wisbey, P.S. Goodwin, F. Langlais, H.M. Flower, J.G. Zheng, D.P. Davies, Mechanical and microstructural behaviour of a particulate reinforced steel for structural applications, Mater. Sci. Technol. 16 (11−12) (2000) 1453–1464.
[24] H. Weiland, J. Nardiello, S. Zaefferer, S. Cheong, J. Papazian, D. Raabe, Microstructural aspects of crack nucleation during cyclic loading of AA7075-T651, Eng. Fract. Mech. 76 (5) (2009) 709–714.
[25] R. Rana, High modulus steels, Can. Metall. Q. 53 (3) (2014) 241–242.
[26] M. Dammak, M. Gaspérini, D. Barbier, Microstructural evolution of iron based metal–matrix composites submitted to simple shear, Mater. Sci. Eng. A 616 (2014) 123–131.
[27] S.G. Song, N. Shi, G.T. Gray, J.A. Roberts, Reinforcement shape effects on the fracture behavior and ductility of particulate-reinforced 6061-Al matrix composites, Metall. Mater. Trans. A 27 (11) (1996) 3739–3746.
[28] P. Shanthraj, M.A. Zikry, Optimal microstructures for martensitic steels, J. Mater. Res. 27 (12) (2012) 1598–1611.
[29] J. Segurado, C. González, J. Llorca, A numerical investigation of the effect of particle clustering on the mechanical properties of composites, Acta Mater. 51 (8) (2003) 2355–2369.
[30] J. Segurado, J. Llorca, Computational micromechanics of composites: The effect of particle spatial distribution, Mech. Mater. 38 (8–10) (2006) 873–883.
[31] A. Ayyar, G.A. Crawford, J.J. Williams, N. Chawla, Numerical simulation of the effect of particle spatial distribution and strength on tensile behavior of particle reinforced composites, Comput. Mater. Sci. 44 (2) (2008) 496–506.
[32] Y. Brechet, J.D. Embury, S. Tao, L. Luo, Damage initiation in metal matrix composites, Acta Metall. Mater. 39 (8) (1991) 1781–1786.
[33] C.H. Caceres, J.R. Griffiths, Damage by the cracking of silicon particles in an Al-7Si-0.4Mg casting alloy, Acta Mater. 44 (1) (1996) 25–33.
[34] J. Llorca, An analysis of the influence of reinforcement fracture on the strength of discontinuously-reinforced metal-matrix composites, Acta Metall. Mater. 43 (1) (1995) 181–192.
[35] M. Kouzeli, L. Weber, C. San Marchi, A. Mortensen, Influence of damage on the tensile behaviour of pure aluminium reinforced with ≥40 vol. pct alumina particles, Acta Mater. 49 (18) (2001) 3699–3709.
[36] R. Jamaati, S. Amirkhanlou, M.R. Toroghinejad, B. Niroumand, Effect of particle size on microstructure and mechanical properties of composites produced by ARB process, Mater. Sci. Eng. A 528 (4–5) (2011) 2143–2148.
[37] J.N. Hall, J. Wayne Jones, A.K. Sachdev, Particle size, volume fraction and matrix strength effects on fatigue behavior and particle fracture in 2124 aluminum-SiCp composites, Mater. Sci. Eng. A 183 (1) (1994) 69–80.
[38] L.C. Davis, C. Andres, J.E. Allison, Microstructure and strengthening of metal matrix composites, Mater. Sci. Eng. A 249 (1–2) (1998) 40–45.
[39] A. Hauert, A. Rossoll, A. Mortensen, Particle fracture in high-volume-fraction ceramic-reinforced metals: governing parameters and implications for composite failure, J. Mech. Phys. Solids 57 (11) (2009) 1781–1800.
[40] F. Roters, P. Eisenlohr, C. Kords, D.D. Tjahjanto, M. Diehl, D. Raabe, DAMASK: the Düsseldorf Advanced MAterial Simulation Kit for studying crystal plasticity using an FE based or a spectral numerical solver, Procedia IUTAM 3 (0) (2012) 3–10.
[41] F. Roters, M. Diehl, P. Shanthraj, P. Eisenlohr, C. Reuber, S.L. Wong, T. Maiti, A. Ebrahimi, T. Hochrainer, H.-O. Fabritius, S. Nikolov, M. Friák, N. Fujita, N. Grilli, K.G.F. Janssens, N. Jia, P.J.J. Kok, D. Ma, F. Meier, E. Werner, M. Stricker, D. Weygand, D. Raabe, DAMASK - the Düsseldorf advanced material simulation kit for modeling multi-physics crystal plasticity, thermal, and damage phenomena from the single crystal up to the component scale, Comput. Mater. Sci. (2018) (in press).
[42] P. Shanthraj, L. Sharma, B. Svendsen, F. Roters, D. Raabe, A phase field model for damage in elasto-viscoplastic materials, Comput. Methods Appl. Mech. Eng. 312 (2016) 167–185.
[43] D. Peirce, R.J. Asaro, A. Needleman, Material rate dependence and localized deformation in crystalline solids, Acta Metall. 31 (12) (1983) 1951–1976.

[44] P. Shanthraj, B. Svendsen, L. Sharma, F. Roters, D. Raabe, Elasto-viscoplastic phase field modelling of anisotropic cleavage fracture, J. Mech. Phys. Solids 99 (2017) 19–34.
[45] M. Diehl, M. Wicke, P. Shanthraj, F. Roters, A. Brueckner-Foit, D. Raabe, Coupled crystal plasticity–phase field fracture simulation study on damage evolution around a void: pore shape versus crystallographic orientation, JOM 69 (5) (2017) 872–878.
[46] B. Bourdin, G.A. Francfort, J.J. Marigo, Numerical experiments in revisited brittle fracture, J. Mech. Phys. Solids 48 (4) (2000) 797–826.
[47] P. Kim, A. Hanen, M. Jean-Jacques, M. Corrado, Gradient damage models and their use to approximate brittle fracture, Int. J. Damage Mech. 20 (4) (2010) 618–652.
[48] B. Bourdin, C.J. Larsen, C.L. Richardson, A time-discrete model for dynamic fracture based on crack regularization, Int. J. Fract. 168 (2) (2011) 133–143.
[49] C. Miehe, F. Aldakheel, A. Raina, Phase field modeling of ductile fracture at finite strains: a variational gradient-extended plasticity-damage theory, Int. J. Plast. 84 (2016) 1–32.
[50] S.M. Allen, J.W. Cahn, A microscopic theory for antiphase boundary motion and its application to antiphase domain coarsening, Acta Metall. 27 (6) (1979) 1085–1095.
[51] P. Eisenlohr, M. Diehl, R.A. Lebensohn, F. Roters, A spectral method solution to crystal elasto-viscoplasticity at finite strains, Int. J. Plast. 46 (0) (2013) 37–53.
[52] P. Shanthraj, P. Eisenlohr, M. Diehl, F. Roters, Numerically robust spectral methods for crystal plasticity simulations of heterogeneous materials, Int. J. Plast. 66 (2015) 31–45.
[53] P. Shanthraj, M. Diehl, P. Eisenlohr, F. Roters, Spectral solvers for crystal plasticity and multi-physics simulations, in: Chun-Hway Hsueh, Siegfried Schmauder, Yutaka Kagawa (Eds.),Mechanics of Materials, Micromechanics, 2017.
[54] H. Moulinec, P. Suquet, A fast numerical-method for computing the linear and nonlinear mechanical-properties of composites, C. R. Acad Sci II 318 (11) (1994) 1417–1423.
[55] H. Moulinec, P. Suquet, A numerical method for computing the overall response of nonlinear composites with complex microstructure, Comput. Methods Appl. Mech. Eng. 157 (1–2) (1998) 69–94.
[56] R.A. Lebensohn, N-site modeling of a 3D viscoplastic polycrystal using Fast Fourier Transform, Acta Mater. 49 (14) (2001) 2723–2737.
[57] S.B. Lee, R.A. Lebensohn, A.D. Rollett, Modeling the viscoplastic micromechanical response of two-phase materials using Fast Fourier Transforms, Int. J. Plast. 27 (5) (2011) 707–727.
[58] R.A. Lebensohn, A.K. Kanjarla, P. Eisenlohr, An elasto-viscoplastic formulation based on fast Fourier transforms for the prediction of micromechanical fields in polycrystalline materials, Int. J. Plast. 32–33 (Suppl. C) (2012) 59–69.
[59] M. Diehl, High-Resolution Crystal Plasticity Simulations, Apprimus Wissenschaftsverlag, 2016.
[60] A. Prakash, R.A. Lebensohn, Simulation of micromechanical behavior of polycrystals: finite elements versus fast Fourier transforms, Model. Simul. Mater. Sci. Eng. 17 (6) (2009), 064010. .
[61] B. Liu, D. Raabe, F. Roters, P. Eisenlohr, R.A. Lebensohn, Comparison of finite element and fast Fourier transform crystal plasticity solvers for texture prediction, Model. Simul. Mater. Sci. Eng. 18 (8) (2010), 085005. .
[62] D.J. Eyre, G.W. Milton, A fast numerical scheme for computing the response of composites using grid refinement*, Eur. Phys. J. Appl. Phys. 6 (1) (1999) 41–47.
[63] J.C. Michel, H. Moulinec, P. Suquet, A computational method based on augmented Lagrangians and fast Fourier Transforms for composites with high contrast, Comput. Model. Eng. Sci. 1 (2) (2000) 79–88.
[64] R.A. Lebensohn, J.P. Escobedo, E.K. Cerreta, D. Dennis-Koller, C.A. Bronkhorst, J.F. Bingert, Modeling void growth in polycrystalline materials, Acta Mater. 61 (18) (2013) 6918–6932.
[65] V. Monchiet, G. Bonnet, A polarization-based FFT iterative scheme for computing the effective properties of elastic composites with arbitrary contrast, Int. J. Numer. Methods Eng. 89 (11) (2011) 1419–1436.
[66] S. Brisard, L. Dormieux, FFT-based methods for the mechanics of composites: a general variational framework, Comput. Mater. Sci. 49 (3) (2010) 663–671.
[67] J. Zeman, J. Vondřejc, J. Novák, I. Marek, Accelerating a FFT-based solver for numerical homogenization of periodic media by conjugate gradients, J. Comput. Phys. 229 (21) (2010) 8065–8071.
[68] M.D. Rintoul, S. Torquato, Reconstruction of the structure of dispersions, J. Colloid Interface Sci. 186 (2) (1997) 467–476.
[69] J.P. Myles, E.C. Flenley, N.R.J. Fieller, H.V. Atkinson, H. Jones, Statistical tests for clustering of second phases in composite materials, Philos. Mag. A 72 (2) (1995) 515–528.
[70] N. Yang, J. Boselli, I. Sinclair, Simulation and quantitative assessment of homogeneous and inhomogeneous particle distributions in particulate metal matrix composites, J. Microsc. (Oxford) 201 (2001) 189–200.
[71] J. Boselli, P.D. Pitcher, P.J. Gregson, I. Sinclair, Secondary phase distribution analysis via finite body tessellation, J. Microsc. (Oxford) 195 (1999) 104–112.
[72] V. Milman, M.C. Warren, Elastic properties of TiB2 and MgB2, J. Phys. Condens. Matter 13 (24) (2001) 5585.
[73] A.K. Shurin, V.E. Panarin, Phase Equilibria and Structure of Alloys of Iron with TiB2, ZrB2 and HfB2, Izv. Akad. Nauk SSSR, Met. 5 (5) (1974) 235–239.
[74] ArcelorResearchGroup, Bulletin 2008/11, 2008 20.
[75] C.C. Tasan, M. Diehl, D. Yan, C. Zambaldi, P. Shanthraj, F. Roters, D. Raabe, Integrated experimental–simulation analysis of stress and strain partitioning in multiphase alloys, Acta Mater. 81 (2014) 386–400.
[76] C.C. Tasan, J.P.M. Hoefnagels, M. Diehl, D. Yan, F. Roters, D. Raabe, Strain localization and damage in dual phase steels investigated by coupled in-situ deformation experiments and crystal plasticity simulations, Int. J. Plast. 63 (2014) 198–210.
[77] M. Diehl, P. Shanthraj, P. Eisenlohr, F. Roters, Neighborhood influences on stress and strain partitioning in dual-phase microstructures, Meccanica 51 (2) (2016) 429–441.
[78] H. Zhang, H. Springer, R. Aparicio-Fernández, D. Raabe, Improving the mechanical properties of Fe – TiB2 high modulus steels through controlled solidification processes, Acta Mater. 118 (Suppl. C) (2016) 187–195.
[79] A.K. Shurin, V.E. Panarin, Phase equilibria and structure of alloys of iron with TiB2, ZrB2 and HfB2, Russ. Metall. (5) (1974) 192–195.
[80] C. Baron, H. Springer, D. Raabe, Effects of Mn additions on microstructure and properties of Fe–TiB2 based high modulus steels, Mater. Des. 111 (Suppl. C) (2016) 185–191.
[81] A. Szczepaniak, H. Springer, R. Aparicio-Fernández, C. Baron, D. Raabe, Strengthening Fe – TiB2 based high modulus steels by precipitations, Mater. Des. 124 (Suppl. C) (2017) 183–193.
[82] J.J. Lewandowski, C. Liu, W.H. Hunt, Effects of matrix microstructure and particle distribution on fracture of an aluminum metal matrix composite, Mater. Sci. Eng. A 107 (1989) 241–255.
[83] D.J. Lloyd, Aspects of fracture in particulate reinforced metal matrix composites, Acta Metall. Mater. 39 (1) (1991) 59–71.
[84] D.L. Davidson, Fatigue and fracture toughness of aluminium alloys reinforced with SiC and alumina particles, Composites 24 (3) (1993) 248–255.
[85] J.J. Williams, Z. Flom, A.A. Amell, N. Chawla, X. Xiao, F. De Carlo, Damage evolution in SiC particle reinforced Al alloy matrix composites by X-ray synchrotron tomography, Acta Mater. 58 (18) (2010) 6194–6205.
[86] Z. Hadjem-Hamouche, K. Derrien, E. Héripré, J.P. Chevalier, In-situ experimental and numerical studies of the damage evolution and fracture in a Fe-TiB2 composite, Mater. Sci. Eng. A 724 (2018) 594–605.
[87] C. Sun, M. Song, Z. Wang, Y. He, Effect of particle size on the microstructures and mechanical properties of SiC-reinforced pure aluminum composites, J. Mater. Eng. Perform. 20 (9) (2011) 1606–1612.
[88] J.J. Lewandowski, 3.07 - fracture and fatigue of particulate MMCs, in: A. Kelly, C. Zweben (Eds.),Comprehensive Composite Materials, Pergamon, Oxford 2000, pp. 151–187.
[89] Y.Z. Li, M.X. Huang, J. Li, J.-Y. Hwang, Interfacial strength characterization in a high-modulus low-density steel-based Fe-TiB2 composite, in: S. Ikhmayies, B. Li, J.S. Carpenter, S.N. Monteiro, D. Firrao, M. Zhang, Z. Peng, J.P. Escobedo-Diaz, C. Bai, Y.E. Kalay, R. Goswami, J. Kim (Eds.), Characterization of Minerals, Metals, and Materials 2017, Springer International Publishing, Cham 2017, pp. 453–460.
[90] M. Dammak, I. Ksaeir, O. Brinza, M. Gasperini, Experimental Analysis of Damage of Fe-TiB2 Metal Matrix Composites Under Complex Loading, 21ème Congrès Français de Mécanique, Bordeaux, 2013.
[91] J. Yang, S.M. Pickard, C. Cady, A.G. Evans, R. Mehrabian, The stress/strain behavior of aluminum matrix composites with discontinuous reinforcements, Acta Metall. Mater. 39 (8) (1991) 1863–1869.